Lipid droplet biogenesis is a liquid phase separation spatially regulated by seipin and membrane curvature.

Valeria Zoni[1], Pablo Campomanes[1], Rasha Khaddaj[1], Abdou Rachid Thiam[2], Roger Schneiter[1] and Stefano Vanni[1,*]

[1] University of Fribourg, Department of Biology, 1700 Fribourg, Switzerland

[2] Laboratoire de Physique de l'Ecole Normale Supérieure, ENS, Université PSL, CNRS, Sorbonne Université , Université de Paris, Paris, France

.

***Correspondence to**:
Stefano Vanni
University of Fribourg
Department of Biology
Chemin du Musée 10
1700 Fribourg
stefano.vanni@unifr.ch

Abstract

Cells store energy in the form of neutral lipids packaged into micrometer-sized organelles named lipid droplets (LDs). These structures emerge from the endoplasmic reticulum (ER), but their biogenesis remains poorly understood. Using molecular simulations, we found that LD formation proceeds via a liquid-liquid phase separation process that is modulated by the physical properties and lipid composition of the ER membrane. LD formation is promoted at ER sites characterized by high membrane curvature and by the presence of the ER-associated protein seipin, that cause accumulation of triglycerides by slowing down their diffusion in the membrane. Our data indicate how a combination of membrane physical properties and protein scaffolding is used by the cell to regulate a broad and energetically-efficient biophysical process such as liquid/liquid phase separation to achieve LD biogenesis.

Lipid droplets (LD) are ubiquitous intracellular organelles that consist of a core of fat molecules, mostly triglycerides (TGs) and sterol esters (SEs), surrounded by a phospholipid monolayer[1]. Because of this unique composition, they are the cellular sites responsible for energy and lipid storage and they play a central role in lipid and cellular metabolism[1–4]. LDs emerge from the endoplasmic reticulum (ER), where the neutral lipids (NLs) constituting them are synthetized by acyltransferases that are essential for LD formation[5]. These early LDs have been observed with electron microscopy (EM), showing an oblate lens-like structure with diameters of 40-60 nm[6]. The early steps of LD biogenesis, however, remain largely unexplored and our understanding of how LDs form [3,4,7–12] is based solely on the extrapolation of sparse experimental observations in reconstituted systems. First, micrometer-sized oil blisters have been observed during the formation of black lipid membranes[13,14] or after addition of TGs to Giant Unilamellar Vesicles[15]. Second, molecular dynamics (MD) simulations have suggested that oil lenses can form between the two bilayer leaflets when the ratio between oil and phospholipids exceeds a certain threshold[16]. These observations have led to a model that posits that LDs form from the spontaneous accumulation of NLs between the two leaflets of the ER into nanometer-sized lipid lenses, before a subsequent maturation that involves LD growth and budding[3,4,7–12]. The current model, however, appears to be at odds with cellular observations in which NLs fail to cluster into LDs, rather accumulating in the ER[17] or in non-native NL-enriched membraneous structures[18]. These phenotypes, caused by deletion of proteins such as the lipid phosphatase Pah1p[17] or the membrane-shaping protein Pex30 together with seipin[18], strongly suggest the presence of regulatory mechanisms modulating LD biogenesis rather than spontaneous NL aggregation.

Given the small length scales of the process and the difficulty of controlling the ratio between NL and phospholipids in both cellular and reconstituted approaches, we investigated the mechanism of LD biogenesis using *in silico* MD simulations. To do so, we built lipid bilayers with increasing concentrations of TG (from 2% to 10%). We initially distributed the TG molecules randomly between the two leaflets of the membrane (Figure 1A) and we let the systems run towards equilibrium. Lens formation took place starting at TG concentrations above 4% following a concentration-dependent nucleation process (Figure 1B). Since both TGs and lipid bilayers can adopt a liquid state at physiological temperature, we hypothesized that LD formation could proceed via a liquid/liquid phase separation (LLPS) process. LLPS is characterized by two main requirements: (i) the two phases must be liquid and (ii) the process must be driven by the equilibrium concentration (e.g. the chemical potential) of the solute (TG, in our case) in the diluted phase[19].

To test the first requirement, we first computed the diffusion of TG molecules in both the diluted phase (the ER membrane) and the condensed phase (the oil blister), and we observed that TG molecules are able to freely diffuse in both phases (Movie S1) with diffusion rates comparable to those of phospholipids (Table S1). Next, we tested whether oil blisters in bilayers can coalesce using three different computational assays: first, we observed that during spontaneous blister formation at high TG concentration (10%), multiple small lenses that initially formed in the simulation coalesced over time to a single one (Figure 1C). Second, we prepared a configuration with 4 identical lenses and observed the formation of a single lens over time (Figure 1D, S1A). Third, we prepared a system with a big lens surrounded by 12 small lenses. Again, we observed their spontaneous coalescence, in this case accompanied by Ostwald ripening. (Figure 1E, S1B, movie S2).

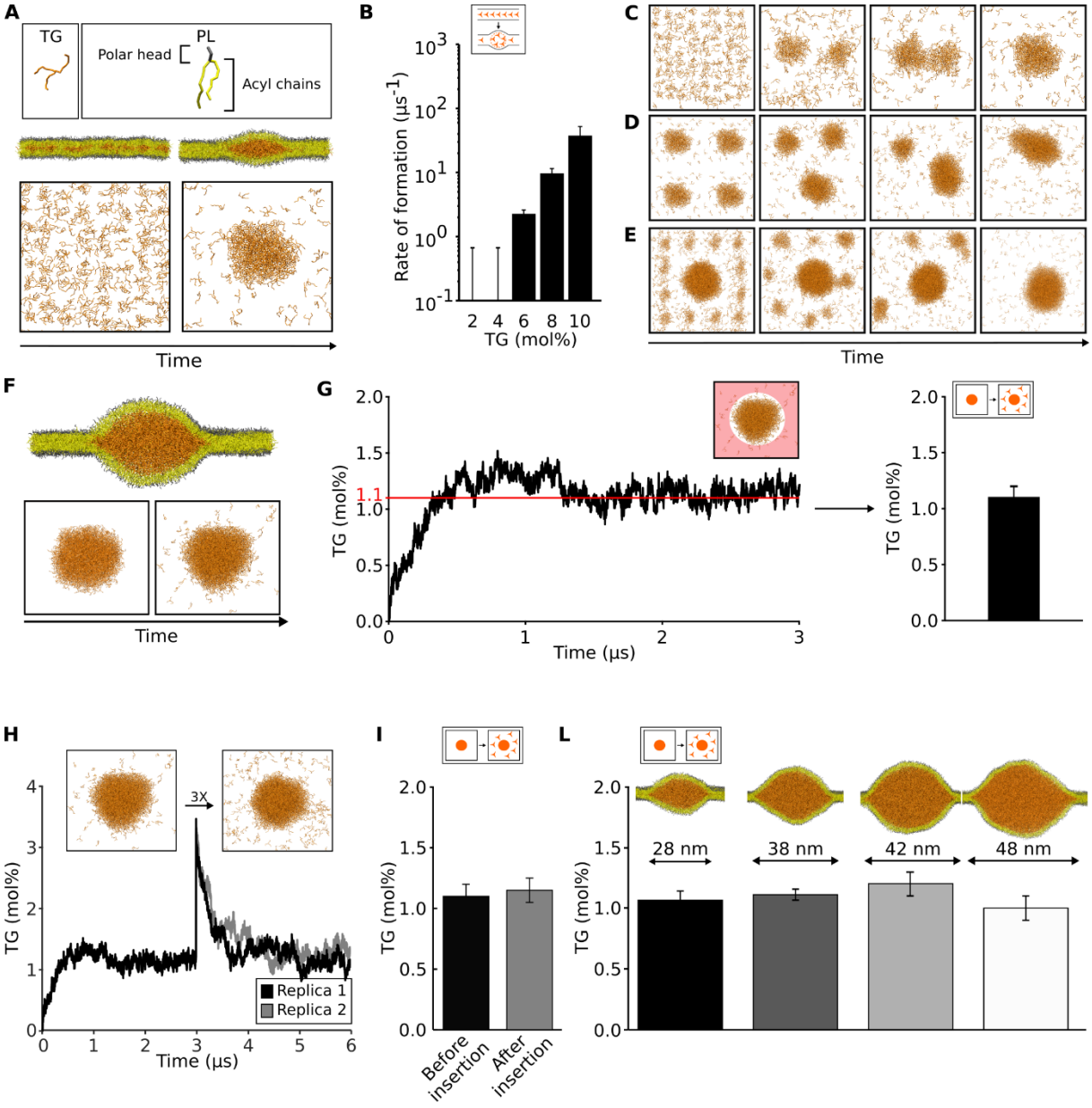

Figure 1. Oil blisters in lipid bilayers form via a liquid/liquid phase separation process. (A) Setup of the nucleation system. (B) Rate of formation of oil lenses at different TG%. (C-E) Coalescence of oil lenses in different MD simulations. (F) Setup of diffusion simulations to quantify the amount of diluted TG and (G) quantification over time. The area in which the diluted TG is measured is highlighted in light red. (H) Quantification of the injection of additional TG molecules and measurement of diluted TG over time. (I) Comparison between the values of diluted TG before and after the insertion of excess TG in the bilayer. (L) Quantification of diluted TG in systems of different sizes.

To test the second requirement, *i.e.* whether the process is driven by the chemical potential of TG in the diluted phase, we first prepared a system that allowed us to

estimate the concentration of TG molecules in a lipid bilayer. To do so, we packed all TG molecules in a pre-formed lens inside a lipid bilayer (Figure 1F) and we followed the time evolution of the concentration of TG molecules spreading into the bilayer (Figure 1F,G). After an initial equilibration, the system reached an equilibrium at the concentration of 1.1±0.1 mol% (Figure 1G, S2), in close agreement with experimental values reported using capacitance measurements[14] or NMR[20].

To test whether the TG concentration in the bilayer is the driving force between the LLPS, we used two different approaches. First, we arbitrarily increased the concentration of the diluted TG in the bilayer by computationally “injecting” new TG molecules in an equilibrated system (Figure 1H). When the system reached equilibrium, all excess TG molecules translocated to the oil lens, with the bilayer TG concentration returning to its initial value after few microseconds (Figure 1H,I). Second, we prepared oil lenses of different sizes compatible with the ones observed using EM[6], ranging from 25 to 50 nm in diameter (Figure 1L). We observed that the concentration of equilibrium TG in the bilayer is independent of the blister size. Finally, when TG blisters with a total TG concentration below the computed chemical potential (1.1% TG/PL) were simulated, this led to blister dissolution (Movie S3). Taken together, our results indicate that indeed oil blister formation in lipid bilayers can be considered as a *bona fide* LLPS.

LLPS is a ubiquitous cellular strategy to achieve membrane-free intracellular compartmentalization[19]. The underlying molecular mechanisms governing the precise spatial regulation of these processes in cellular systems, however, remain mostly elusive, but the establishment of nucleation sites where the local concentration of the solute is higher than in its surroundings is a common requirement[19]. We hypothesized that in our specific case, solvent properties (i.e. characteristics of the ER membrane)

together with the activity of specific ER-embedded proteins, could control the localization of LD formation by promoting LLPS at specific ER sites.

We first tested whether ER properties could modulate the propensity for blister formation and, concomitantly, the concentration of TG molecules residing in the ER membrane. We first tested whether ER physical properties, such as low membrane tension and widespread membrane curvature, might also modulate this mechanism. We observed that increasing membrane tension antagonizes blister formation, by both decreasing its rate (Figure 2B) and by increasing the amount of diluted TG in bilayers (Figure 2C), in agreement with in vitro experiments[15]. Membrane curvature, on the other hand, didn't appear to affect blister formation rate (Figure 2E), nor the chemical potential of TG molecules (Figure 2F).

Next, we investigated the effect of lipids that are either relatively abundant in the ER, such as those carrying unsaturated chains, phosphatidyl-ethanolamine (PE) or those that are precursors of NLs, such as DAG and cholesterol (Figure 2G)[21,22]. Lipid unsaturation slightly promotes blister formation, as does the presence of PE lipids (Figure 2H). A more pronounced effect towards blister formation was observed in the case of the NL precursors, with even mild concentrations of DAG and cholesterol promoting phase separation at low (<4%) TG concentrations (Figure 2H). Since deletion of Pah1p, the lipid phosphatase converting PA in DAG upstream of TAG synthesis, results in a phenotype where NLs are present in the cell at significant concentration but fail to cluster into LDs and rather accumulate in the ER[17], our data suggest that a local increase in the membrane concentration of DAG, the precursor of TG, could promote LD biogenesis at specific ER sites enriched in Pah1p.

Taken together, our results suggest that the ER membrane appears engineered to promote oil blister formation, allowing only very low concentration of diluted TG in the

ER (Figure 2I), possibly to reduce TG-induced lipotoxicity. Indeed, a lipid composition mimicking that of the ER showed the lowest concentration of diluted TG and the highest blister formation rates, including at low TG concentration (Figures 2H,I).

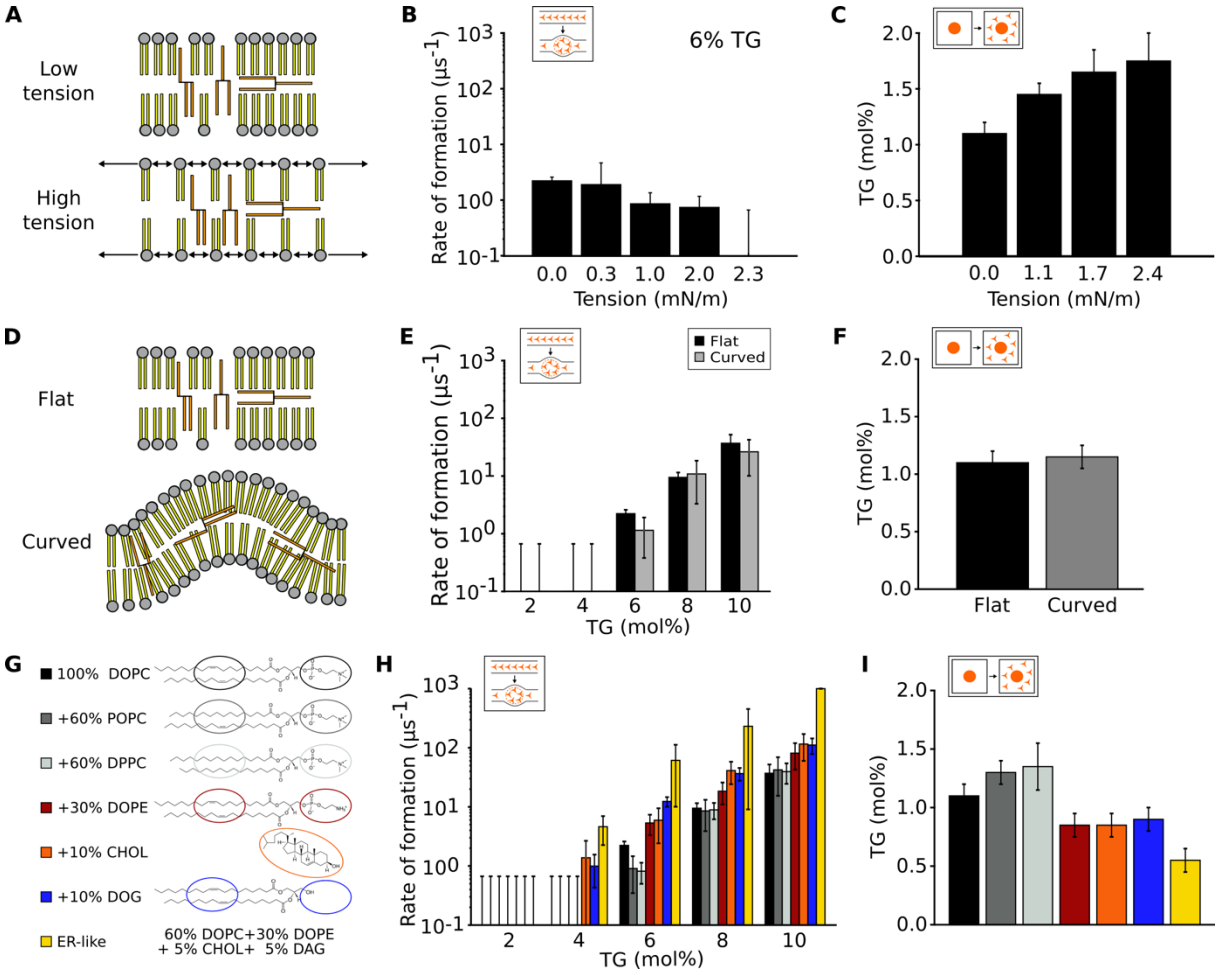

Figure 2: ER properties promote LD biogenesis. (A) Cartoon of the TG-enriched bilayer at different tensions. (B) Rate of formation and (C) diluted TG quantification at different surface tensions. (D) Cartoon of flat and curved bilayers containing TG. (E) Rate of formation and (F) diluted TG quantification in curved systems. (G) Chemical representation of various lipid compositions tested and corresponding (H) rates of blister formation and (I) diluted TG quantification.

The observation that membrane curvature doesn't promote blister formation appears to be at odds with the recent experimental observation of a prominent role of membrane-shaping proteins in LD formation[18,23]. We reasoned, however, that if LD biogenesis occurs via a LLPS that is triggered by the TG concentration in the ER, as our simulations suggest (Figure 1B), it would be possible to increase the local TG concentration by slowing down its diffusion in predetermined ER sites.

To investigate this possibility, we first ruled out that physicochemical membrane properties such as membrane tension or presence of specific lipids slows down TG diffusion (Table S1). We noticed, however, that in highly curved tubular structures mimicking ER tubules (Figure 3A), equilibration of TG molecules inside the tubule was much slower than in flat bilayers (Figure 3B). We thus computed the diffusion of TG molecules along the radial and axial coordinates of the tubule, and we found that diffusion along the radial axis was significantly slower in comparison with that along the axial coordinate or with that in flat bilayers (Figure 3C), similarly to what has been shown for the diffusion of phospholipids in curved membranes[24]. To further test this hypothesis, we measured the distribution of TG molecules in lipid bilayers with coexisting flat and curved patches as a function of membrane curvature, at TG levels below the critical concentration for nucleation (Figure 3D). We observed that the concentration of TG molecules is up to 2-fold higher in regions of high curvature when compared to flat regions (Figure 3D). At higher TG concentrations, when spontaneous formation of oil blisters was observed, lens invariantly nucleated at sites of high curvature, remaining there throughout the entire simulation (Figure 3E).

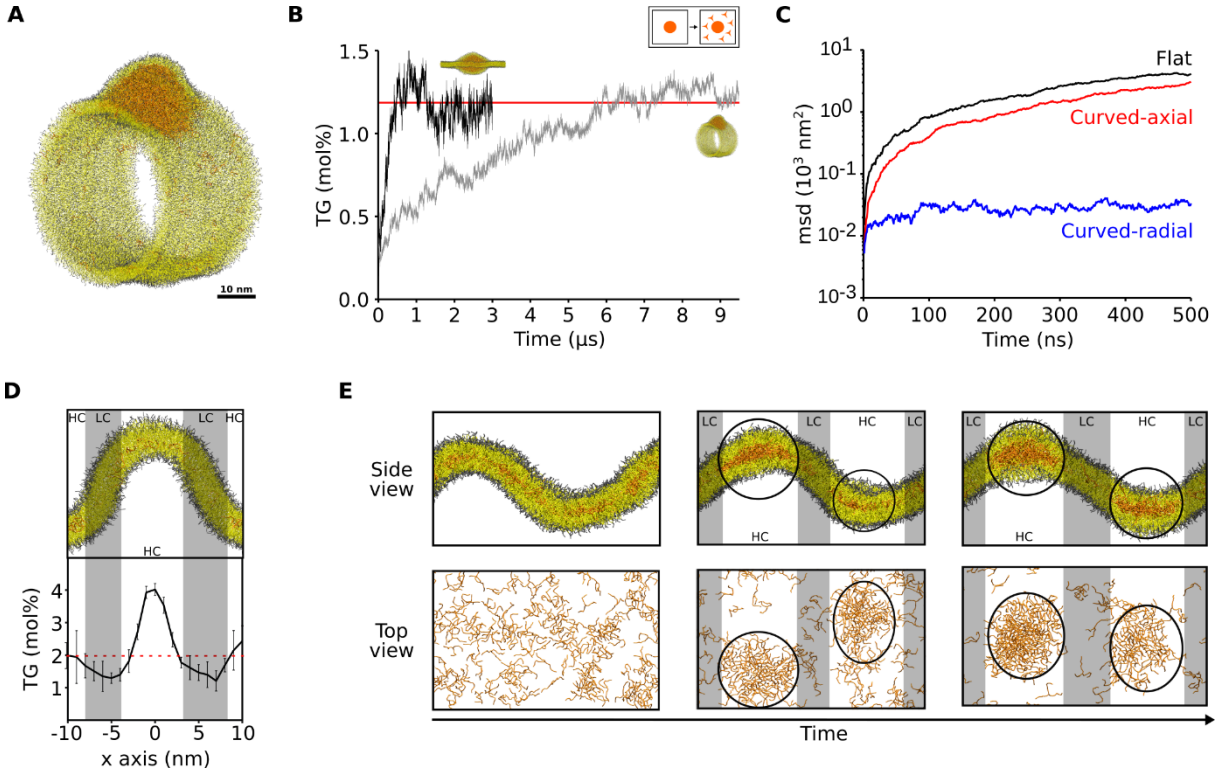

Figure 3: Membrane curvature slows down TG diffusion. (A) Snapshot from the MD simulation of a membrane tubule with an embedded nascent TG blister. (B) Equilibration of the diluted TG concentration over time in tubular and flat systems. (C) Mean square displacement of TG molecules at low concentration (2 mol%) in different systems: flat bilayer (black), along the axial coordinate of the membrane tubule (red) and along the radial coordinate of the membrane tubule (blue). (D) Quantification of TG concentration as a function of membrane curvature. Regions of high curvature (HC) are highlighted in white, while regions of low curvature (LC) are highlighted in gray. (E) Snapshots of blister formation in curved system. Oil blisters are highlighted with black circles.

The membrane-shaping protein Pex30 has been shown to promote LD biogenesis in cooperation with the ER-resident protein seipin[18,23]. We thus reasoned that the seipin oligomer (Figure 4A) could also cooperate with membrane curvature to slow down the diffusion of TGs in its proximity due to lipid-protein interactions. Of note, seipin has been recently shown to mark the sites of LD formation[25], and stand-alone deletion of seipin has been shown to lead to NL accumulation in the ER and delayed LD formation[26]. To test this hypothesis we first prepared a model of the transmembrane region of seipin based on the recently determined cryo-EM structures of the soluble part of seipin [27,28] and we embedded this model in a large membrane patch with 2% TG (Figure 4A,B). We next measured the concentration of TG molecules as a function

of the distance from the protein complex, and we found that interactions between the TG molecules and the seipin complex raise the local concentration of TG in the proximity of the protein to 4%, twice the initial value in the bulk membrane (Figure 4C,D) in our MD simulations. This increase in local concentration is due to a decrease in TG diffusion in proximity of the protein (Figure E,F), analogously to what has been shown for diffusion of lipids around proteins[29].

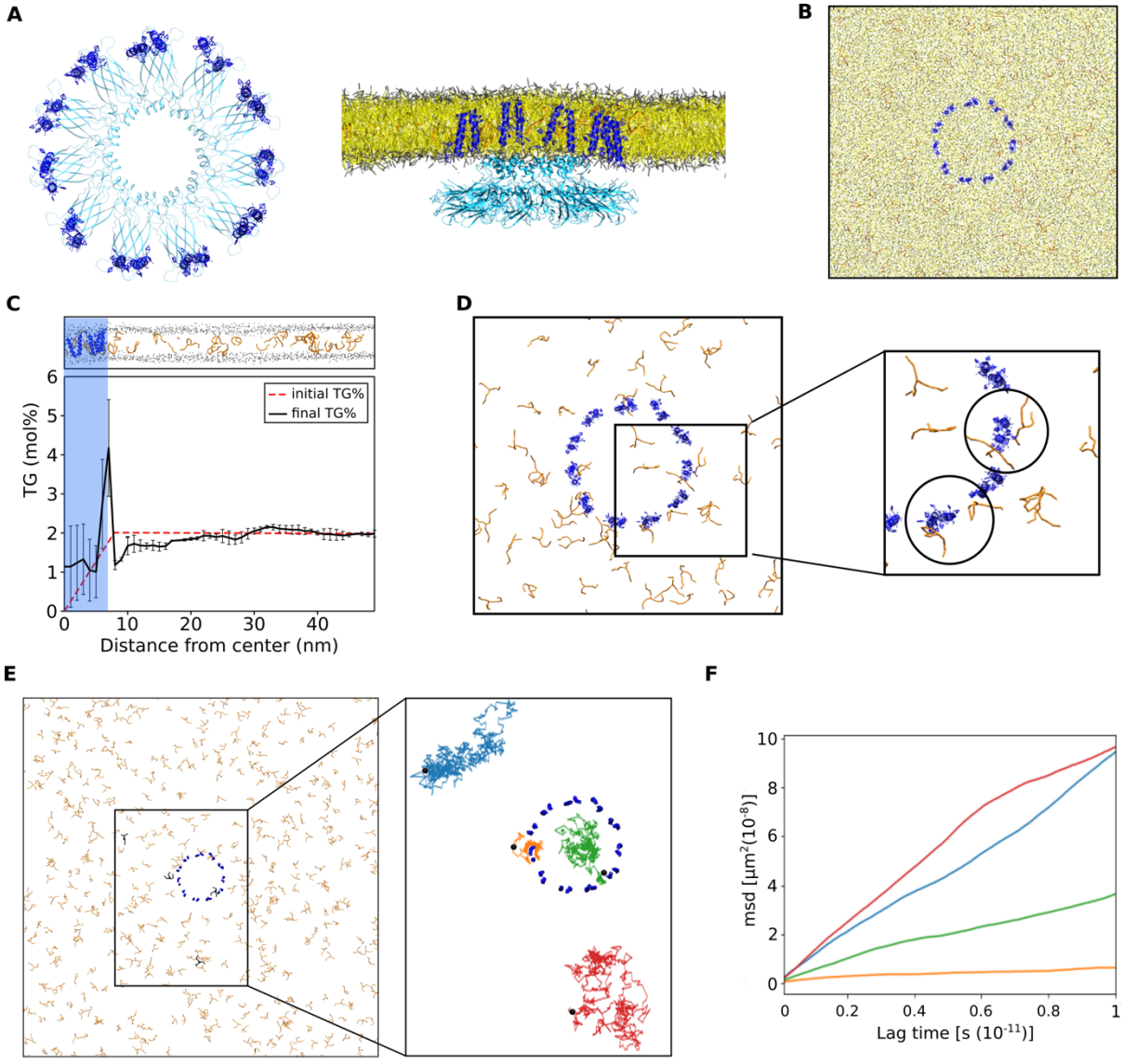

Figure 4: The seipin oligomer clusters TG molecules. (A) Top and side view of the seipin structure from EM (light blue) and of the TM helices modeled for the simulations (blue). (B) Setup of the MD simulations with seipin and TG. (C) Quantification of TG% as a function of the distance from the center of the seipin ring. (D) MD screenshot showing TG molecules trapped between seipin TMs. (E) Starting position (black) and single trajectories of 4 representative TG molecules: two that are far from seipin (red and blue lines), one that is trapped into the seipin circular structure (green) and one that is trapped closed to seipin (orange). (F) Mean square diffusion of the 4 molecules along time.

Our observations suggest that the mechanism of LD biogenesis is a LLPS process arising from the accumulation of NLs between the two leaflets of the ER. This model is consistent with multiple cellular observations showing a diffuse localization of NLs inside the ER[17,18,26], and with the role of Pex30 and seipin in marking the sites of LD biogenesis[18,25]. This process provides a highly-efficient framework, since all newly-synthetized excess NLs in the ER will translocate to LDs without the need of *ad-hoc* protein machineries and energy consumption other than their biosynthesis, while retaining high spatial selectivity. Our investigations provide a conceptual framework for the investigation of the spatial localization of LLPS inside the cell.

Methods

Molecular dynamics (MD) simulations

The MD simulations containing only lipids were performed using the software LAMMPS[30] and employing the Shinoda-Devane-Klein (SDK) force field [31–34]. Combination rules, as described in [35], were used to derive non-bonded interactions of DAG with DOPE and cholesterol. Initial configurations and input files were obtained through conversion of atomistic snapshots using the CG-it software (https://github.com/CG-it/).

For the systems containing the protein Seipin, GROMACS software[36] was used to perform MD in combination with the MARTINI2 force field [37]. TG was mapped according to [16].

In the simulations run with LAMMPS, pressure and temperature were controlled via a Nosé-Hoover thermostat[38] and barostat[39–41]: target temperature was 310K and average pressure was 1 atm. The lateral *xy* dimensions were coupled, while the *z*

dimension was allowed to fluctuate independently. Temperature was dumped every 0.4 ps, while pressure every 1 ps. Linear and angular momenta were removed every 100 timesteps. In systems with non-zero surface tension, the *xy* dimensions were kept fixed with no pressure-coupling. Van der Waals and electrostatic interaction were truncated at 1.5 nm. Long-range electrostatics beyond this cutoff were computed using the particle-particle-particle-mesh (PPPM) solver, with an RMS force error of 10^{-5} kcal mol^{-1} $Å^{-1}$ and order 3. In all CG-SDK systems, a time step of 20 fs was used, except for bilayers containing cholesterol, where a time step of 10 fs was used.

For the simulations containing Seipin, pressure was controlled through a Parrinello-Rahman barostat[38,39] and temperature through a thermostat that uses velocity rescaling with a stochastic term[42]. Target pressure and temperature were set at 1 bar and 310K. Pressure was coupled every 12 ps, with a compressibility constant of $3x10^{-4}$ bar^{-1} and temperature was coupled every 1 ps. Van der Waals and electrostatic interactions cutoffs were fixed at 1.1 nm. A time step of 20 fs was used.

MD systems setups

In order to study the formation of TG lenses (Figure 1A-B), bilayers containing different concentrations of TG were studied. To build the system, a box consisting of 50 phospholipids (PLs) molecules and a variable number of TG molecules corresponding to the different TG concentrations was initially prepared. The two PL monolayers were displaced along the z-axis in order to allow the insertion of the TG molecules without any steric contact between the molecules. The TG molecules were subsequently randomly placed between the two monolayers. The box was then replicated 8 times along the x and y axis for a total of 3200 PL molecules in each system. Different bilayer compositions were tested, as reported in Table 1. Simulations were run until

spontaneous lens formation (see *MD simulations analysis* for details*)* or for a total of 1.5 us per run if no spontaneous lens formation was observed (Table 1).

For the study of coalescence processes, two additional systems were built. For the first one (Figure 1D), we replicated 4 times the coordinates from the last snapshot of the simulation with DOPC and 10% TG (radius 7 nm, last panel Figure 1C). For the second, we used the coordinates from the last step of the simulation to calculate "free TG" (see below) and the ones from the last snapshot of the simulation of TG lenses formation with DOPC and 6% TG, in order to have a big lens (14 nm radius) in the center surrounded by 12 small lenses with a radius of 5 nm (Figure 1E).

To simulate systems with tension > 0 mN/m (Figure 2A-B), systems containing 3200 DOPC and 192 TG molecules were minimized and equilibrated for 1 ns, then, for 250 ps, the box was increased gradually in *x* and *y* dimensions using different scaling factors to obtain different values of tension. Then, the obtained systems were run keeping *x* and *y* dimensions fixed. The same protocol was applied to bigger systems in order to study the effect of tension on the concentration of "free TG" (see below, Figure 2C).

The curved systems (Figure 2E, 3D and 3E) were created by building bilayers of 1600 DOPC molecules containing different concentration of TG uniformly distributed. After equilibration, a force along the *x* direction was applied and then *x* and *y* dimensions were kept fixed during the production, as described in [43]. The curvature radii were computed using MATLAB scripts.

To calculate the concentration of diluted TG in the bilayer (Figure 1F-G, 1I and Figure 2I), systems were formed by positioning a lens of 1836 TG molecules between two monolayers with 3025 DOPC lipids each, as in [15]. We also created bigger systems with 12250 lipids and 1836, 5508 or 9180 TG molecules or 16200 DOPC and 13665 TG, in

order to study the size independence of the concentration of diluted TG in the bilayer at equilibrium. The bilayer compositions described in Table 1 were tested.

The tubular bilayer was obtained from a DOPC vesicle built using Packmol software[44]: a central circular crown of 5 nm length was isolated and replicated 10 times. The crowns were then placed 1 nm apart and the system was run without restraints leading to spontaneous self-assembly of the tubular structure. The obtained tubule was equilibrated and small holes were used to equilibrate the number of lipids in the inner/outer monolayers. The holes were created by applying a cylindric indenter of radius 3 nm to the beads corresponding to the polar head of PLs. Then, the monolayers of a small portion of the tubule were separated in order to allow the insertion of a lens of 1794 TG molecules. The system was further equilibrated until complete reconstruction of the tubular structure and then the simulation was run for additional 9.5 μs. We kept the holes open to allow equilibration of the lipids between the two monolayers.

To study the effect of inserting new TG molecules in the bilayer (Figure 1H) we built systems from the coordinate file of the last frame of one of the two simulations used to computed the amount of diluted TG (Figure 1F,G). The two bilayers were slightly separated from TG in the *z* direction using TCL scripts and only the molecules considered as outside the lens (see section *MD simulations analysis*) were replicated 3 times using the tool for VMD TopoTools Plugin [Axel Kohlmeyer, (2017)].

The system with the protein seipin (UniProt reference number: Q96G97) was built using the program Packmol. The all atom representation of the transmembrane helices of Seipin were built with the plugin Molefacture present in VMD and then coarse grained using CHARMM-gui tools[45]. An elastic network, defined using MARTINI2 standard parameters for force constant and cutoffs, was used to keep the secondary

structure of the helices. The position of the transmembrane helices was obtained from the coordinates of the terminal residues of the cryoEM structure of human Seipin, present in the PDB data bank with the code 6D5S[27]. After a short 10 ps equilibration without restraints and subsequent 4 ns equilibration with positional restraint along all the directions (Fc=1000 kj/mol nm^2), positional restraints of Fc=1000 kj/mol nm^2 along *x* and *y* directions were applied to the helices in order to maintain a circular conformation consistent with the cryoEM structure. Seipin was positioned in a DOPC bilayer containing 2% TG.

TG lenses formation				
System	Bilayer composition (N of molecules)	N of TG	N of replicas	Length (μs)
100% DOPC	3200 DOPC	64	3	1.5
	3200 DOPC	128	3	1.5
	3200 DOPC	192	3	< 1.5
	3200 DOPC	256	3	< 1.5
	3200 DOPC	320	3	< 1.5
+60% POPC	1280 DOPC + 1920 POPC	64	3	1.5
	1280 DOPC + 1920 POPC	128	3	1.5
	1280 DOPC + 1920 POPC	192	3	< 1.5
	1280 DOPC + 1920 POPC	256	3	< 1.5
	1280 DOPC + 1920 POPC	320	3	< 1.5
+ 60% DPPC	1280 DOPC + 1920 DPPC	64	3	1.5
	1280 DOPC + 1920 DPPC	128	3	1.5
	1280 DOPC + 1920 DPPC	192	3	< 1.5
	1280 DOPC + 1920 DPPC	256	3	< 1.5
	1280 DOPC + 1920 DPPC	320	3	< 1.5
+30% DOPE	2240 DOPC + 960 DOPE	64	3	1.5
	2240 DOPC + 960 DOPE	128	3	1.5
	2240 DOPC + 960 DOPE	192	3	< 1.5
	2240 DOPC + 960 DOPE	256	3	< 1.5
	2240 DOPC + 960 DOPE	320	3	< 1.5
+10% CHOL	2880 DOPC + 320 CHOL	64	3	1.5
	2880 DOPC + 320 CHOL	128	3	< 1.5
	2880 DOPC + 320 CHOL	192	3	< 1.5
	2880 DOPC + 320 CHOL	256	3	< 1.5
	2880 DOPC + 320 CHOL	320	3	< 1.5
+10% DAG	2880 DOPC + 320 DAG	64	3	1.5
	2880 DOPC + 320 DAG	128	3	< 1.5
	2880 DOPC + 320 DAG	192	3	< 1.5
	2880 DOPC + 320 DAG	256	3	< 1.5

	2880 DOPC + 320 DAG	320	3	< 1.5
+20% DOG	2560 DOPC + 640 DAG	64	3	1.5
	2560 DOPC + 640 DAG	128	3	< 1.5
	2560 DOPC + 640 DAG	192	3	< 1.5
	2560 DOPC + 640 DAG	256	3	< 1.5
	2560 DOPC + 640 DAG	320	3	< 1.5
ER like	1856 DOPC + 960 DOPE + 192 CHOL + 192 DAG	64	3	1.5
	1856 DOPC + 960 DOPE + 192 CHOL + 192 DAG	128	3	< 1.5
	1856 DOPC + 960 DOPE + 192 CHOL + 192 DAG	192	3	< 1.5
	1856 DOPC + 960 DOPE + 192 CHOL + 192 DAG	256	3	< 1.5
	1856 DOPC + 960 DOPE + 192 CHOL + 192 DAG	320	3	< 1.5
Curved DOPC	1600 DOPC	32	3	1.5
	1600 DOPC	64	3	1.5
	1600 DOPC	96	3	< 1.5
	1600 DOPC	128	3	< 1.5
	1600 DOPC	160	3	< 1.5
Tension > 0 mN/m	3200 DOPC	64	3	1.5
	3200 DOPC	128	3	1.5
	3200 DOPC	192	3	< 1.5
	3200 DOPC	256	3	< 1.5
	3200 DOPC	320	3	< 1.5
Coalescence				
System 1	8276 DOPC	1172	2	9
System 2	11349 DOPC	2672	2	>9
Calculation of "free TG"				
100% DOPC	6050 DOPC	1836	2	3
+ 60% POPC	2410 DOPC + 3630 POPC	1836	2	3
+ 60% DPPC	2410 DOPC + 3630 DPPC	1836	2	3
+ 30% DOPE	4235 DOPC + 1815 DOPE	1836	2	3
+10% CHOL	5445 DOPC + 605 CHOL	1836	2	3
+10% DAG	5445 DOPC + 605 DAG	1836	2	3
ER like	3509 DOPC + 1815 DOPE + 363 DAG + 363 CHOL	1836	2	3
+20% DAG	4840 DOPC + 1210 DAG	1836	2	3
+20% CHOL	4840 DOPC + 1210 CHOL	1836	2	3
Tension > 0 mN/m	6050 DOPC	1836	2	3
Tubular DOPC	11770 DOPC	1794	2	9.5
Insertion of TG	6050 DOPC	1836	2	3
Different sizes	11250 DOPC	1836	2	3
	11250 DOPC	5508	2	3
	11250 DOPC	9180	2	3
	16200 DOPC	13665	2	3
Seipin				

seipin	28800 DOPC	567	3	4
Diffusion				
Tubular DOPC	11272 DOPC	235	1	0.5
Dissolution				
Dissolution	6050 DOPC	50	1	0.8

Table 1. List of all the MD setups, with bilayer composition, number of TG molecules, number of replicas and length of simulations.

MD simulations analysis

The formation of a triglyceride lens was determined according to the following algorithm: an aggregate of at least 25 TG molecules within 3.5 nm of a TG molecule, that was stable for at least 5 ns. The simulations were run until formation of a TG lens or for 1.5 μs if no aggregation occurred. For each TG concentration, bilayer composition and setup, 3 independent simulations were performed. Rate of formation is calculated as the inverse of the time of formation, obtained from the average over the three replicas. Error bars are computed from error propagation from standard deviation of time of formation from the three independent simulations. For simulations where no formation was observed, error bars are given as the inverse of the total simulation time (1.5 μs).

The analysis of the concentration of diluted TG was performed using the following algorithm: first, we defined as part of the lens all the TG molecules that are within 5 nm of another TG molecule and not within 2.8 nm of the PLs. The “free bilayer” was defined as all lipid molecules that are at least 2.5 nm far away from the lens. We tested different selections and the chosen one allowed us to consider the widest area of free bilayer, excluding the side of the lens where TG molecules move continuously inside and outside the lens (Figure S2). Except for the tubular structure, the simulations were run for 3 μs (see Table 1). The percentage of TG molecules inside the bilayer was obtained averaging the values of the last 1.5 μs of simulation, while the error bars are obtained

from the standard deviation over two independent simulations. The dimensions of TG lenses were calculated using the minimum and the maximum *x*, *y* and *z* coordinates of the TG molecules at each side of the lens, averaged over time.

The concentration of TG in the curved systems (figure 3D) was obtained by dividing the box in slices of 1 nm along the *x* axis and by counting the number of TG and DOPC molecules in each region. The percentage of TG was obtained averaging the values of 300 ns of simulation for three different replicas, while the error bars are obtained from the standard deviation over the three independent simulations.

In the systems containing Seipin, TG mol% vs distance from the center of the seipin ring was calculated dividing the bilayer in annuli delimited by concentric circles of radius=R+1 nm and counting the number of TG and DOPC molecules in each region. The percentage of TG was obtained averaging the values of 1.5 μs of simulation for three different replicas, while the error bars are obtained from the standard deviation over the three independent simulations. Trajectories of single molecules and mean squared displacement for 4 selected TG molecules were calculated using the tool Trackpy (https://soft-matter.github.io/trackpy/v0.3.2/).

Mean squared displacement (MSD) of TG and DOPC molecules were obtained using the LAMMPS command “compute msd” during production. For the tubular system, axial and radial MSD were calculated using the following equation:

$$MSD = \langle (x_t - x_0)^2 \rangle$$

Being the axis of our cylinder oriented toward y, for the axial diffusion coefficient, x_t is the coordinate y of the particles at time *t* and x_0 is the coordinate y at the reference point *t*=0. For the radial diffusion, x_t is the radial coordinate ρ ($\rho^2 = x^2 + z^2$) at time *t* and

x_0 is the radial coordinate ρ at t=0. Then, diffusion coefficients were calculated using the script msd2diff.py available in the ELBA-LAMMPS toolkit (https://github.com/orsim/elba-lammps/tree/master/tools).

For all simulations, surface tension was computed from the diagonal values of the pressure tensor (Pxx, Pyy, and Pzz) using the Kirkwood-Irving method:

$$g = \frac{L}{2} < P_{zz} - \frac{1}{2}\left(P_{xx} + P_{yy}\right) >$$

where L is the box length in the z dimension and <> means an ensemble average.

All molecular images were rendered using VMD software[46] and the graph produced with the software MATLAB.

Acknowledgments

We thank Vikram Reddy and Vineet Choudhary for useful discussions. This work was supported by the Swiss National Science Foundation (grant #163966). This work was supported by grants from the Swiss National Supercomputing Centre (CSCS) under project ID s726 and s842. We acknowledge PRACE for awarding us access to Piz Daint, ETH Zurich/CSCS, Switzerland.

References

1. Walther, T. C. & Farese Jr, R. V. Lipid Droplets and Cellular Lipid Metabolism. *Annu. Rev. Biochem.* **81**, 687–714 (2012).
2. Gao, Q. & Goodman, J. M. The lipid droplet — a well-connected organelle. *Front. Cell Dev. Biol.* **3**, 49 (2015).
3. Pol, A., Gross, S. P. & Parton, R. G. Biogenesis of the multifunctional lipid droplet : Lipids , proteins , and sites. *J. Cell Biol.* **204**, 635–646 (2014).
4. Olzmann, J. A. & Carvalho, P. Dynamics and functions of lipid droplets. *Nat. Rev. Mol. Cell Biol.* **20**, 137–155 (2019).
5. Sandager, L. *et al.* Storage lipid synthesis is non-essential in yeast. *J. Biol. Chem.* **277**, 6478–6482 (2002).
6. Choudhary, V., Ojha, N., Golden, A. & Prinz, W. A. A conserved family of proteins facilitates nascent lipid droplet budding from the ER. *J. Cell Biol.* **211**, 261–271 (2015).
7. Walther, T. C., Chung, J. & Farese Jr, R. V. Lipid Droplet Biogenesis. *Annu. Rev. Cell Dev. Biol.* **33**, 1–20 (2017).
8. Joshi, A. S., Zhang, H. & Prinz, W. A. Organelle biogenesis in the endoplasmic reticulum. *Nat. Cell Biol.* **19**, 876–882 (2017).
9. Sturley, S. L. & Hussain, M. M. Lipid droplet formation on opposing sides of the endoplasmic reticulum. *J. Lipid Res.* **53**, 1800–1810 (2012).
10. Thiam, A. R. & Beller, M. The why, when and how of lipid droplet diversity. *J. Cell Sci.* **130**, 315–324 (2017).
11. Chen, X. & Goodman, J. M. The collaborative work of droplet assembly. *Biochimica et Biophysica Acta - Molecular and Cell Biology of Lipids* **1862**, 1205–1211 (2017).
12. Thiam, A. R. & Forêt, L. The physics of lipid droplet nucleation, growth and budding. *Biochim. Biophys. Acta - Mol. Cell Biol. Lipids* **1861**, 715–722 (2016).
13. White, S. H. Studies of the physical chemistry of planar bilayer membranes using high-precision measurements of specific capacitance. *Ann. N. Y. Acad. Sci.* **303**, 243–265 (1977).
14. White, S. H. The physical nature of planar bilayer membranes. in *Ion Channel Reconstitution* 3–35 (1986).
15. M'barek, K. Ben *et al.* ER Membrane Phospholipids and Surface Tension

Control Cellular Lipid Droplet Formation. *Dev. Cell* **41**, 591–604 (2017).

16. Khandelia, H., Duelund, L., Pakkanen, K. I. & Ipsen, J. H. Triglyceride Blisters in Lipid Bilayers: Implications for Lipid Droplet Biogenesis and the Mobile Lipid Signal in Cancer Cell Membranes. *PLoS One* **5**, e12811 (2010).
17. Adeyo, O. *et al.* The yeast lipin orthologue Pah1p is important for biogenesis of lipid droplets. *J. Cell Biol.* **192**, 1043–1055 (2011).
18. Wang, S. *et al.* Seipin and the membrane-shaping protein Pex30 cooperate in organelle budding from the endoplasmic reticulum. *Nat. Commun.* **9**, 2939 (2018).
19. Hyman, A. A., Weber, C. A. & Frank, J. Liquid-Liquid Phase Separation in Biology. *Annu. Rev. Cell Dev. Biol.* **30**, 39–58 (2014).
20. Hamilton, J. A., Miller, K. W. & Small, D. M. Solubilization of Triolein and Cholesteryl Oleate in Egg Phosphatidylcholine Vesicles*. *J. Biol. Chem.* **258**, 12821–12826 (1983).
21. Penno, A., Hackenbroich, G. & Thiele, C. Phospholipids and lipid droplets. *Biochim. Biophys. Acta - Mol. Cell Biol. Lipids* **1831**, 589–594 (2013).
22. Tauchi-Sato, K., Ozeki, S., Houjou, T., Taguchi, R. & Fujimoto, T. The Surface of Lipid Droplets Is a Phospholipid Monolayer with a Unique Fatty Acid Composition. *J. Biol. Chem.* **277**, 44507–44512 (2002).
23. Joshi, A. S. *et al.* A family of membrane-shaping proteins at ER subdomains regulates pre-peroxisomal vesicle biogenesis. *J. Cell Biol.* **215**, 515 LP – 529 (2016).
24. Risselada, H. J. & Marrink, S. J. Curvature effects on lipid packing and dynamics in liposomes revealed by coarse grained molecular dynamics simulations. *Phys. Chem. Chem. Phys.* **11**, 2056–2067 (2009).
25. Salo, V. T. *et al.* Seipin Facilitates Triglyceride Flow to Lipid Droplet and Counteracts Droplet Ripening via Endoplasmic Reticulum Contact. *Dev. Cell* (2019).
26. Cartwright, B. R. *et al.* Seipin performs dissectible functions in promoting lipid droplet biogenesis and regulating droplet morphology. *Mol. Biol. Cell* **26**, 726–739 (2014).
27. Yan, R. *et al.* Human SEIPIN Binds Anionic Phospholipids. *Dev. Cell* **47**, 248-256.e4 (2018).
28. Sui, X. *et al.* Cryo–electron microscopy structure of the lipid droplet–formation

protein seipin. *J. Cell Biol.* **217**, 4080 LP – 4091 (2018).

29. Niemelä, P. S. *et al.* Membrane Proteins Diffuse as Dynamic Complexes with Lipids. *J. Am. Chem. Soc.* **132**, 7574–7575 (2010).
30. Plimpton, S. Fast Parallel Algorithms for Short–Range Molecular Dynamics. *J. Comput. Phys.* **117**, 1–19 (1995).
31. Shinoda, W., DeVane, R. & Klein, M. L. Multi-property fitting and parameterization of a coarse grained model for aqueous surfactants. *Mol. Simul.* **33**, 27–36 (2007).
32. Bacle, A., Gautier, R., Jackson, C. L., Fuchs, P. F. J. & Vanni, S. Interdigitation between Triglycerides and Lipids Modulates Surface Properties of Lipid Droplets. *Biophys. J.* 1417–1430 (2017).
33. MacDermaid, C. M. *et al.* Molecular dynamics simulations of cholesterol-rich membranes using a coarse- grained force field for cyclic alkanes. *J. Chem. Phys.* **143**, 243144 (2015).
34. Campomanes, P., Zoni, V. & Vanni, S. Local accumulation of diacylglycerol alters membrane properties nonlinearly due to its transbilayer activity. *Commun. Chem.* **2**, 72 (2019).
35. Macdermaid, C. M. *et al.* Molecular dynamics simulations of cholesterol-rich membranes using a coarse- grained force field for cyclic alkanes. *J. Chem. Phys. J. Chem. Phys. J. Chem. Phys. J. Chem. Phys.* **143**, 243144–243112 (2015).
36. Abraham, M. W. M., Hess, B., Van Der Spoel, D. & Lindahl, E. *GROMACS User Manual version 2018*. (2018).
37. Marrink, S. J., Risselada, H. J., Yefimov, S., Tieleman, D. P. & De Vries, A. H. The MARTINI force field: Coarse grained model for biomolecular simulations. *J. Phys. Chem. B* **111**, 7812–7824 (2007).
38. Nosé, S. A molecular dynamics method for simulations in the canonical ensemble. *Mol. Phys.* **52**, 255–268 (1984).
39. Parrinello, M. & Rahman, A. Polymorphic transitions in single crystals: A new molecular dynamics method. *J. Appl. Phys.* **52**, 7182–7190 (1981).
40. Martyna, G. J., Tobias, D. J. & Klein, M. L. Constant pressure molecular dynamics algorithms. *J. Chem. Phys.* **101**, 4177–4189 (1994).
41. Shinoda, W., Shiga, M. & Mikami, M. Rapid estimation of elastic constants by molecular dynamics simulation under constant stress. *Phys. Rev. B* **69**, 134103

(2004).

42. Bussi, G., Donadio, D. & Parrinello, M. Canonical sampling through velocity rescaling. *J. Chem. Phys.* **126**, 014101 (2007).
43. Hu, M., Diggins, P., Deserno, M. & Diggins, P. I. Determining the bending modulus of a lipid membrane by simulating buckling. *J. Chem. Phys. J. Chem. Phys. J. Chem. Phys. J. Chem. Phys.* **138**, 214110–164109 (2013).
44. Martínez, L., Andrade, R., Birgin, E. G. & Martínez, J. M. Packmol: A Package for Building Initial Configurations for Molecular Dynamics Simulations. (2009).
45. Jo, S., Kim, T., Iyer, V. G. & Im, W. CHARMM-GUI: A web-based graphical user interface for CHARMM. *J. Comput. Chem.* **29**, 1859–1865 (2008).
46. Humphrey, W., Dalke, A. & Schulten, K. VMD: Visual Molecular Dynamics.